Optics Letters

Excitation of Bloch-like surface waves in quasi-crystals and aperiodic dielectric multilayers

Vijay Koju[1],* and **William M. Robertson[1,2]**

[1]Computational Science Program, Middle Tennessee State University, 1301 E. Main St., Murfreesboro, Tennessee 37132, USA
[2]Department of Physics and Astronomy, Middle Tennessee State University, 1301 E. Main St., Murfreesboro, Tennessee 37132, USA
*Corresponding author: vk2g@mtmail.mtsu.edu

The existence of Bloch surface waves in periodic dielectric multilayer structures with a surface defect is well known. Not yet recognized is that quasi-crystals and aperiodic dielectric multilayers can also support Bloch-like surface waves. In this work, we numerically show the excitation of Bloch-like surface waves in Fibonacci quasi-crystals and Thue–Morse aperiodic dielectric multilayers using the prism coupling method. We report improved surface electric field intensity and penetration depth of Bloch-like surface waves in the air side in such structures compared to their periodic counterparts. © 2016 Optical Society of America

OCIS codes: (240.6690) Surface waves; (310.4165) Multilayer design; (310.6845) Thin film devices and applications.

http://dx.doi.org/10.1364/OL.41.002915

Following the prediction [1] and experimental realization [2] of Bloch surface waves (BSWs)—electromagnetic modes propagating at the interface of truncated dielectric multilayer structures and a homogeneous medium—in photonic crystals, these modes have been studied and experimentally observed in various photonic crystal configurations [3–5]. However, the photonic crystals explored previously were all periodic in nature with a surface defect. This inclination toward periodic crystals for excitation of BSWs is largely due to the establishment of their robust and well-understood theoretical background and advances in fabrication techniques that can be applied to such crystals. Moreover, despite the significant interest in optical characteristics of quasi-crystals and deterministically aperiodic photonic crystals, it has not yet been recognized that such structures can also support Bloch-like surface waves (BLSWs). Other optical properties of these aperiodic systems, such as dispersion and bandgaps [6,7], perfect transmission [8,9], propagation [10,11] and localization [12,13] of light, have been extensively studied. It is observed that when compared to their periodic counterparts, quasi-crystals and aperiodic multilayers exhibit enhanced optical properties and also add significant flexibility in optical engineering [14]. Recognizing this fact, we numerically show the excitation of BLSWs in Fibonacci quasi-crystals (FQC) and Thue–Morse aperiodic dielectric multilayer (TMADM) structures. The advantage of FQCs and TMADMs

over the conventional periodic dielectric multilayers (PDMs) is twofold. First, the electric field (E-field) intensity at the surface due to BLSWs in FQCs and TMADMs is significantly improved compared to their periodic counterparts. This improved surface field intensity can be utilized for engineering optical slow light devices [15], slow light enhanced nonlinear effects [16,17], surface-enhanced Raman spectroscopy [18,19], label-free biosensing based on enhanced diffraction [20–22], spectral and angular resonance shift [23,24], and fluorescence-based detection [25–27]. Second, the penetration depth of the exponentially decaying BLSW in the homogeneous medium is increased. The extended penetration depth results in a higher interaction with the homogeneous medium and, consequently, higher sensitivity to the refractive index change in that medium. This feature, together with the improved surface field intensity of FQCs and TMADMs, can be exploited to make sensitivity enhanced biosensors.

FQCs are well-known examples of one-dimensional quasi-periodic crystals, first proposed by Kohmoto *et al.* [28]. They are designed using a simple substitution rule: $A \rightarrow AB$, $B \rightarrow A$. On the other hand, TMADMs are commonly used aperiodic multilayers [29,30] generated using the inflation rule $A \rightarrow AB$, and $B \rightarrow BA$. The first four generations of FQCs and TMADMs, assuming the first generation (S_0) to be A, are given in Table 1.

In this Letter, we use $TiO_2(A)$ and $SiO_2(B)$ as the high and low refractive index materials. We consider wavelength (λ)-dependent refractive indices of both TiO_2 [31] and SiO_2 [32] over the range of 0.43 to 0.8 μm given by

$$n_{TiO_2}^2 = 5.913 + \frac{0.2441}{\lambda^2 - 0.0803}, \qquad (1)$$

and

$$n_{SiO_2}^2 - 1 = \frac{0.6961663\lambda^2}{\lambda^2 - 0.0684043^2} + \frac{0.4079462\lambda^2}{\lambda^2 - 0.1162414^2} + \frac{0.8974794\lambda^2}{\lambda^2 - 9.896161^2}, \qquad (2)$$

respectively. In the rest of the Letter, however, λ is given in nanometers. We also introduce small dielectric losses in these materials through the imaginary parts of their refractive indices. The values used here, 0.0007 and 0.0001 for TiO_2 and SiO_2, respectively, are based on published sources [33,34] and are

Table 1. First Four Generations of FQCs and TMADMs

Generation (S_j)	FQC	TMADM
S_0	A	A
S_1	AB	AB
S_2	ABA	$ABBA$
S_3	$ABAAB$	$ABBABAAB$

selected to match with experimental investigations of BSWs [3,23,24]. For our study, we use a 34-layered FQC (Fibonacci order $j = 7$) and a 32-layered TMADM (Thue–Morse order $j = 5$) with thicknesses of 71.9 nm and 108.4 nm for the TiO_2 and SiO_2 layers, respectively. These layer thicknesses correspond to quarter-wave stacks at the wavelength 632.8 nm for normal incidence, taking the refractive indices of TiO_2 and SiO_2 to be 2.2 and 1.46, respectively. Similar periodic systems have been extensively studied numerically and experimentally [3,4,23,24]. However, since the structures studied in this Letter are not periodic in nature, the choice is arbitrary; we note that the freedom to choose essentially any values for layer thicknesses creates an enormous parameter space in designing new applications. The number of layers, the layer thicknesses, materials, and the superstrate refractive index are some parameters that can be varied. The exploration of these parameter spaces is amenable only via numerical computation. Our Letter provides a roadmap for discovering and characterizing the surface modes in these systems.

The theoretical model consisting of prism/multilayer/air (Kretschmann configuration) is shown in Fig. 1. Although BSW/BLSW modes are intrinsically present at dielectric–air interfaces, they cannot be directly excited by light incident from the air side due to their nonradiative and evanescent nature. The use of a prism mitigates this inability by providing an additional momentum to the free-space wave vector required to satisfy the phase-matching condition with the BSW/BLSW wave vector.

The coupling of the free-space wave vector into the BLSW wave vector can be realized by observing sharp dips in the reflection maps. In this Letter, the reflection maps of E-field waves in transverse-electric (TE) mode for FQCs and TMADMs are computed from an iterative implementation of Fresnel's equations as a function of angle of incidence (θ_{inc}) and wavelength. For any particular wavelength, at incident angles above the critical angle, the dips in the reflectivity curve represent light coupling either into BLSW modes or inner guided modes. These modes can be distinguished by their characteristic E-field profiles. Knowing the angle of incidence at which BLSW is excited, the field profile can be computed by solving for the E-field
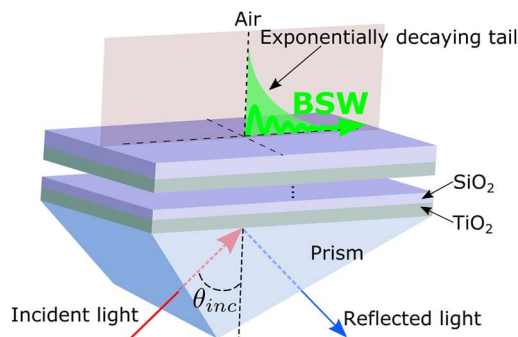
iteratively in the multilayer structure imposing the continuity of the E-field and its derivative at the interfaces. The BLSW modes have a highly confined E-field at the surface layer and an exponentially decaying field profile in the homogeneous superstrate layer. However, unlike the BSW modes, the field confinement of the BLSW modes in the nonhomogeneous multilayer side is not necessarily tied to periodicity, and, thus, they can have nonexponential decaying field profiles. The guided modes, on the other hand, have a confined E-field in the inner layers of the multilayer. To understand the nature of BLSW modes, we also compute their dispersion curves by applying a coordinate transformation for their incidence angle axis given by $k_{BLSW} = (2\pi/\lambda_0)n_p \sin(\theta_{BLSW})$, where k_{BLSW} is the parallel wave vector of BLSW, $n_p = 1.5$ is the refractive index of the prism, and λ_0 and θ_{BLSW} are the free-space wavelength and angle of incidence at the respective BLSW reflectivity minima extracted from the reflection map.

The reflection map of a 34-layered FQC in contact with air is shown in Fig. 2(a). Beyond the light line (dotted line), we observe several optical modes over the wavelength range of 430–800 nm. The BLSW modes are labeled $BLSW_1$ and $BLSW_2$. The remaining modes that lie between $BLSW_1$ and $BLSW_2$ are guided modes in the inner layers of the FQC. In a periodic multilayer, the excitation of BSWs is attributed to the surface defect. The introduction of the surface defect breaks the translational symmetry of the multilayer, which facilitates additional optical modes in the otherwise forbidden bandgaps [35]. The FQC pattern for Fibonacci order $j = 7$ is ABAABABAABAABABAABABAABAABABAABAAB. This sequence is not periodic and thus it does not have translational symmetry. However, the components of this sequence can be subgrouped in a "periodic" form as **XYXYXZ**, where **X = ABAABA**, **Y = BAABAAB**, and **Z = AB**. The subgroup **Z** acts as the surface defect that supports the excitation of the BLSW in this FQC. The dispersion curves of the supported BLSWs are illustrated in Fig. 2(b). The frequency axis is normalized by multiplying the angular frequency (ω) by $a/2\pi c$, where a is the thickness of a unit cell consisting of a TiO_2 and SiO_2 bilayer, and c is the speed of light. A similar normalization for the wave vector axis is accomplished by multiplying the parallel wave vector (k) by $a/2\pi$. The shaded region is the radiative light cone in air, whereas the white region is the nonradiative region. The solid black line that divides the radiative and nonradiative regions is the dispersion line for light incident at the grazing angle along the multilayer surface in the absence of the prism. The BLSW modes (solid red curves) lie beyond the light line in the nonradiative region. Figures 2(c) and 2(d) show the E-field intensity ($|E|^2$) profiles, normalized to the incident E-field intensity ($|E_0|^2 = 1$), overlaid on top of their structure profiles corresponding to $BLSW_2$ and $BLSW_1$, respectively. The E-field intensity in Fig. 2(c) is observed for the incident angle of 45.67° at the wavelength 443.2 nm. The incident angle and wavelength for Fig. 2(d) are 42.14° and 760 nm, respectively. The plots demonstrate that the E-field intensity at the surface is magnified by ∼1500 × and ∼100 × for $BLSW_2$ and $BLSW_1$, respectively. Such high E-field intensity at the surface of multilayer structures is of great significance for fluorescence-based detection [25–27] and surface-enhanced Raman spectroscopy [18,19]. The plots also permit determination of the penetration depth (PD) of the evanescent wave beyond the surface as 93 and 533 nm at the exp(−1) point.
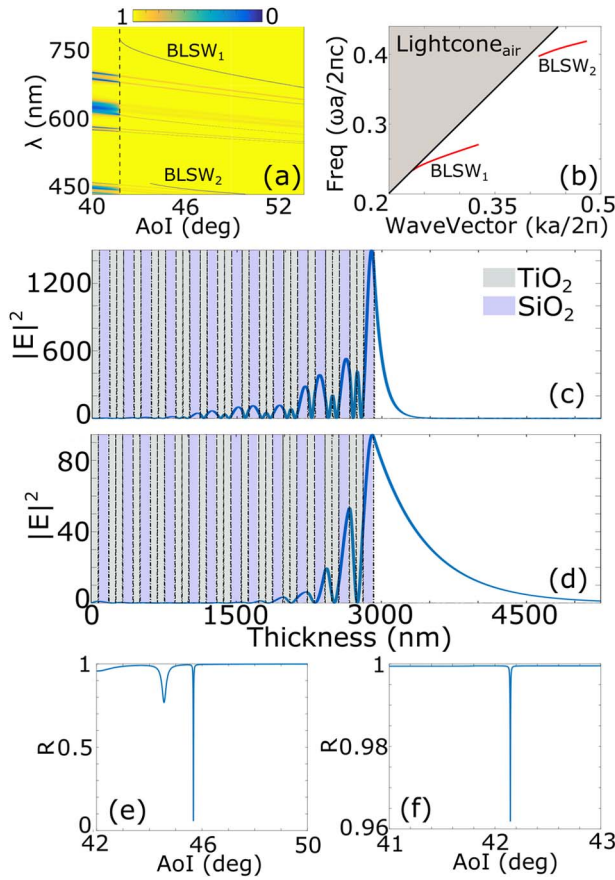

Fig. 1. Schematic of a prism coupling technique (Kretschmann configuration) to excite Bloch surface waves or Bloch-like surface waves using a dielectric multilayer.

Fig. 2. BLSWs in FQC. (a) Reflection map of a 34-layered FQC (Fibonacci order $j = 7$) in contact with air as a function of wavelength (λ) and angle of incidence (AoI). (b) Dispersion curves of $BLSW_1$ and $BLSW_2$. (c) and (d) BLSW assisted E-field intensity at the surface for (c) $\lambda = 443.2$ nm and AoI = 45.67°, and (d) $\lambda = 760$ nm and AoI = 42.14°. (e) and (f) Reflectivity curves as a function of AoI at (e) $\lambda = 443.2$ nm, and (f) $\lambda = 760$ nm.
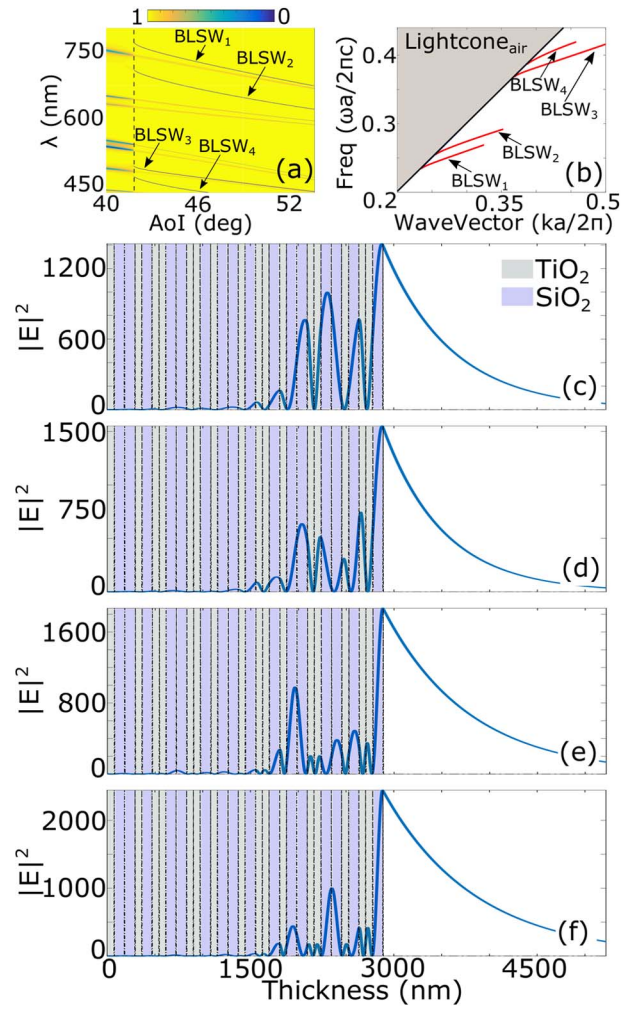

Fig. 3. BLSWs in TMADM. (a) Reflection map of a 32-layered TMADM (Thue–Morse order $j = 5$) in contact with air as a function of λ and AoI. (b) Dispersion curves of $BLSW_1$, $BLSW_2$, $BLSW_3$, and $BLSW_4$. (c)–(f) BLSW assisted E-field intensity at the surface for (c) $\lambda = 762.4$ nm and AoI = 42°, (d) $\lambda = 701.4$ nm and AoI = 42.01°, (e) $\lambda = 488.1$ nm and AoI = 41.86°, and (f) $\lambda = 465.1$ nm and AoI = 41.85°.

Figures 2(e) and 2(f) show the reflectivity dips for the respective BLSW excitations in Figs. 2(c) and 2(d).

Figure 3(a) is the reflection map of a 32-layered TMADM. The BLSW modes lie in the bandgap regions between the optical modes that exist in the inner layers of the TMADM. Their dispersion curves are presented in Fig. 3(b). The TMADM pattern for Thue–Morse order $j = 5$ is ABBABAAB BAAABABBABAAABABBAABBABAAB. Our attempt to find some hidden "periodicity" in the TMADM sequence failed. However, the sequence can be subgrouped in a near-periodic form as **XYXY′XZ**, where **X** = ABBAB, **Y** = AABBAAB, **Y′** = AAABABBA, and **Z** = AAB, with **Z** acting as the surface defect. The subgroups **Y** and **Y′** have the same first three components, but the order of last four components is switched. The sequence can also be subgrouped in other near-periodic forms. The structure pattern and the $|E|^2$ field profiles for the four distinct BLSW modes are illustrated in Figs. 3(c)–3(f). The BLSW in Fig. 3(c) is realized at the incident angle of 42° and wavelength of 762.4 nm. The maximum E-field intensity at the surface and the exp(−1) PD obtained for this mode ($BLSW_1$) are ~1410 × and 710 nm, respectively. E-field intensity of ~1550 × and PD of 630 nm are attained at the $BLSW_2$ mode in Fig. 3(d) for incident angle 42.01° and wavelength

701.4 nm. The E-field intensity and the PD for the $BLSW_3$ in Fig. 3(e) at the incident angle 41.86° and wavelength 488.1 nm are ~1870 × and 894 nm, respectively. Similarly, for the $BLSW_4$ at 41.85° and 465.1 nm [Fig. 3(f)], the E-field intensity and the PD are ~2450 × and 960 nm, respectively. We note that the results presented here are based on an infinite plane wave approach. In real applications, the results will be modified because of finite beam spot size [18].

It is evidenced that the FQCs and TMADMs exhibit enhanced optical properties compared to their periodic counterparts [14]. To compare the surface E-field intensity and the exp(−1) PD obtained from the FQC ($j = 7$) and the TMADM ($j = 5$) with that from a PDM, we plot the $|E|^2$ field profile of a 32-layered PDM in Fig. 4. The PDM consists of alternating layers of TiO_2 and SiO_2 with thicknesses of 71.9 and 108.4 nm, respectively. The surface SiO_2 (defect layer) has a thickness of 120 nm. The BSW wavelength of 440 nm and the incident angle of 54.16° for Fig. 4 are chosen such that
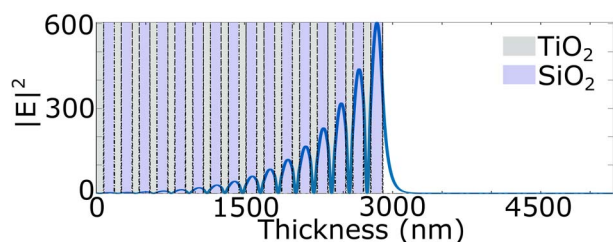
Fig. 4. BSW assisted E-field intensity at the surface of a periodic counterpart (32 layers) of FQC and TMADM at wavelength 440 nm and incident angle 53.16°.

the E-field intensity at the surface of the structure is the largest. For the results presented in Figs. 2, 3, and 4, we do not undergo any optimization. Optimizing the structure parameters, such as layer thicknesses, refractive indices, and number of layers, can improve the results further.

The maximum surface E-field intensities of the BLSWs and the exp(−1) PD obtained for the FQC from Figs. 2(c) and 2(d) and from Figs. 3(c) and 3(f) for the TMADM, along with that for the PDM from Fig. 4, are plotted in Figs. 5(a) and 5(b). The PDM has only one BSW mode over the wavelength range of 430–800 nm, whereas the FQC and the TMADM have two and four BLSW modes, respectively, corresponding to the different number of data points for the PDM, FQC, and TMADM in Figs. 5(a) and 5(b). For the PDM, the maximum E-field intensity at the surface is ∼600 ×, which is low compared to the amplifications of up to 1495 and 2450 obtained in the FQC and the TMADM, respectively. The evanescent tail extending to the air side beyond the PDM surface has exp(−1) PD equal to 55.45 nm, whereas the PD for the FQC and the TMADM are 533 and 961 nm, respectively. We emphasize that this comparison is not comprehensive because we fix the number of layers and the thicknesses of the PDM to be the same as that of the TMADM, and that the structures are not optimized. The increased PD for the FQC and the TMADM results from BLSW resonances near the total internal reflection (TIR) angle. The angle of incidence sets the real part of the k_{BSW} and determines the PD as given by $1/PD \sim (k_{BSW}^2 - k_{air}^2)^{1/2}$. A comparable PD for the PDM can be obtained for BSW resonances near the TIR angle, but for the PDM considered here, we do not observe BSW near the TIR angle. In general, shifting the BSW/BLSW resonance toward the TIR angle increases the PD of these resonances.

In conclusion, we demonstrate the excitation of BLSWs in a 34-layered FQC and a 32-layered TMADM, which, to our knowledge, has not been reported previously. Although these structures are not periodic, their components can be subgrouped to obtain some superficial periodicity, which can potentially
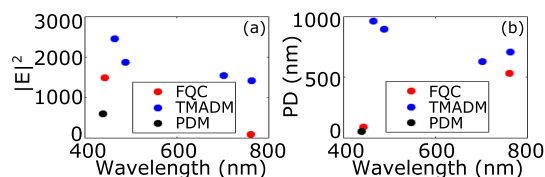

Fig. 5. (a) Maximum E-field intensity at the surface of the 34-layered FQC (red circle), 32-layered TMADM (blue circle), and 32-layered PDM (black circle). (b) Exp(−1) penetration depth beyond the surface of the FQC, TMADM, and PDM into the air side.

explain the excitation of BLSWs in these structures. They possess several advantages over their periodic counterparts. The surface E-field intensity is highly enhanced and the exp(−1) penetration depth in the air side beyond the surface is strongly extended. We envision applications of these enhanced properties in making better slow light devices and highly sensitive BLSW assisted biosensors for analyte refractive index change detection, and improved surface-enhanced Raman spectroscopy.

REFERENCES

1. R. D. Meade, K. D. Brommer, A. M. Rappe, and J. D. Joannopoulos, Phys. Rev. B **44**, 10961 (1991).
2. W. M. Robertson, G. Arjavalingam, R. D. Meade, K. D. Brommer, A. M. Rappe, and J. D. Joannopoulos, Opt. Lett. **18**, 528 (1993).
3. W. M. Robertson and M. S. May, Appl. Phys. Lett. **74**, 1800 (1999).
4. W. M. Robertson, J. Lightwave Technol. **17**, 2013 (1999).
5. G. A. Rodriguez, J. D. Ryckman, Y. Jiao, and S. M. Weiss, Biosens. Bioelectron. **53**, 486 (2014).
6. T. Hattori, N. Tsurumachi, S. Kawato, and H. Nakatsuka, Phys. Rev. B **50**, 4220 (1994).
7. M. A. Kaliteevski, V. V. Nikolaev, R. A. Abram, and S. Brand, Opt. Spectrosc. **91**, 109 (2001).
8. X. Q. Huang, S. S. Jiang, R. W. Peng, and A. Hu, Phys. Rev. B **63**, 245104 (2001).
9. R. Nava, J. Tagüeña, J. A. del Rio, and G. G. Naumis, J. Phys. Condens. Matter **21**, 155901 (2009).
10. N. Liu, Phys. Rev. B **55**, 3543 (1997).
11. M. Ghulinyan, B. J. Oton, L. D. Negro, L. Pavesi, R. Sapienza, M. Colocci, and D. S. Wiersma, Phys. Rev. B **71**, 094204 (2005).
12. W. Gellermann, M. Kohmoto, B. Sutherland, and P. C. Taylor, Phys. Rev. Lett. **72**, 633 (1994).
13. M. Dulea, M. Johansson, and R. Riklund, Phys. Rev. B **45**, 105 (1992).
14. Z. V. Vardeny, A. Nahata, and A. Agrawal, Nat. Photonics **7**, 177 (2013).
15. V. Koju and W. M. Robertson, Opt. Express **22**, 15679 (2014).
16. M. Soljačić and J. D. Joannopoulos, Nat. Mater. **3**, 211 (2004).
17. K. Inoue, H. Oda, N. Ikeda, and K. Asakawa, Opt. Express **17**, 7206 (2009).
18. A. Delfan, M. Liscidini, and J. E. Sipe, J. Opt. Soc. Am. B **29**, 1863 (2012).
19. S. Pirotta, X. G. Xu, A. Delfan, S. Mysore, S. Maiti, G. Dacorro, M. Patrini, M. Galli, G. Guizzetti, D. Dajoni, J. E. Sipe, G. C. Walker, and M. Liscidini, J. Phys. Chem. C **117**, 6821 (2013).
20. M. Liscidini and J. E. Sipe, Appl. Phys. Lett. **91**, 253125 (2007).
21. M. Liscidini, M. Galli, M. Patrini, R. W. Loo, M. C. Goh, C. Ricciardi, F. Fiorgis, and J. E. Sipe, Appl. Phys. Lett. **94**, 043117 (2009).
22. M. Liscidini and J. E. Sipe, Virtual J. Biomed. Opt. **26**, 279 (2009).
23. M. Shinn and W. M. Robertson, Sens. Actuators B **105**, 360 (2005).
24. A. Farmer, A. C. Friedli, S. M. Wright, and W. M. Robertson, Sens. Actuators B **173**, 79 (2012).
25. K. Toma, E. Descrovi, M. Toma, M. Ballarini, P. Mandracci, F. Fiorgis, A. Mateescu, U. Jonas, W. Knoll, and J. Dostálek, Biosens. Bioelectron. **43**, 108 (2013).
26. A. Angelini, E. Enrico, N. D. Leo, P. Munzert, L. Boarino, F. Michelotti, F. Giorgis, and E. Descrovi, New J. Phys. **15**, 073002 (2013).
27. F. Frascella, S. Ricciardi, P. Rivolo, V. Moi, F. Giorgis, E. Descrovi, F. Michelotti, P. Munzert, N. Danz, L. Napione, M. Alvaro, and F. Bussolino, Sensors **13**, 2011 (2013).
28. M. Kohmoto, L. P. Kadanoff, and C. Tang, Phys. Rev. Lett. **50**, 1870 (1983).
29. R. Riklund and M. Severin, J. Phys. C **21**, 3217 (1988).
30. M. Dulea, M. Severin, and R. Riklund, Phys. Rev. B **42**, 3680 (1990).
31. J. R. Devore, J. Opt. Soc. Am. **41**, 416 (1951).
32. I. H. Malitson, J. Opt. Soc. Am. **55**, 1205 (1965).
33. C. C. Ting, S. Y. Chen, and D. M. Liu, J. Appl. Phys. **88**, 4628 (2000).
34. S. Chao, W. H. Wang, and C. C. Lee, Appl. Opt. **40**, 2177 (2001).
35. J. D. Joannopoulos, S. G. Johnson, J. N. Winn, and R. D. Meade, *Photonic Crystals: Molding the Flow of Light* (Princeton University, 2008).